The Astrophysical Journal, 891:150 (11pp), 2020 March 10 https://doi.org/10.3847/1538-4357/ab6dc8

Origins of X-Ray Line Emissions in Circinus X-1 at Very Low X-Ray Flux

N. S. Schulz[1], T. E. Kallman[2], S. Heinz[3], P. Sell[4], P. Jonker[5], and W. N. Brandt[6]
[1] Kavli Institute for Astrophysics and Space Research, Massachusetts Institute of Technology, Cambridge, MA 02139, USA
[2] Goddard Space Flight Center, NASA, Greenbelt, MD, USA
[3] Department of Astronomy, University of Wisconsin, Madison, WI, USA
[4] Department of Physics, University of Crete, Heraklion, Greece
[5] Department of Astrophysics, Radboud University Nijmegen, The Netherlands
[6] Department of Astronomy & Astrophysics, 525 Davey Laboratory, The Pennsylvania State University, University Park, PA 16802, USA
Received 2018 August 21; revised 2019 December 12; accepted 2020 January 15; published 2020 March 13

Abstract

Accretion conditions and morphologies of X-ray transients containing neutron stars are still poorly understood. Circinus X-1 is an enigmatic case where we observe X-ray flux changes covering four orders of magnitude. We observed Circinus X-1 several times at its very lowest X-ray flux using the high-energy transmission grating spectrometer on board the *Chandra X-ray Observatory*. At a flux of 1.8×10^{-11} erg cm^{-2} s^{-1} we observed a single 1.6 keV blackbody spectrum. The observed continuum luminosity of 10^{35} erg s^{-1} is about two orders of magnitude too low to explain the observed photoionized luminosity, suggesting a much more complex structure of the X-ray source that is partially or entirely obscured, as had been previously suggested. This affects most emissions from the accretion disk, including previously observed accretion-disk coronal line emissions. Instead, the strongest observed photoionized lines are blueshifted by about ∼400 km s^{-1}, and we suggest that they originate in the ionized wind of a B5Ia supergiant companion, supporting a previous identification. The neutron star in Cir X-1 is very young and should have a high magnetic field. At the observed luminosity, the emission radius of the blackbody is small enough to be associated with the accretion hot spot as the X-ray-emitting region. The small emission radius then points to a field strength below 10^{12} G, which would be consistent with the observation of occasional type I X-ray bursts at high magnetic fields. We discuss Cir X-1 in the context of being a high-mass X-ray binary, with some emphasis on a possible Be-star X-ray binary nature.

Unified Astronomy Thesaurus concepts: Neutron stars (1108); Accretion (14); X-ray sources (1822); High-mass x-ray binary stars (733)

1. Introduction

Since its discovery in the early days of X-ray astronomy (Margon et al. 1971), Circinus X-1 has shown a vast range of brightness levels, variability patterns, and spectral changes in its X-ray emissions. Despite significant advances in recent years, these emissions remain poorly understood. Until about a decade ago, it appeared fairly well established from the photometric variability of the optical counterpart (Stewart et al. 1991; Glass 1994), its orbital parameters (Brandt & Podsiadlowski 1995; Tauris et al. 1999), as well as its X-ray spectral and timing patterns (Tennant 1987; Shirey et al. 1999) that Cir X-1 is probably a low-mass X-ray binary containing a neutron star. The latter is now well determined through the direct observation of type I X-ray bursts (Tennant et al. 1986) and their recent confirmation (Linares et al. 2010; Papitto et al. 2010). From kinematic parameters and the assumption that Cir X-1 is associated with the supernova remnant G321.9-0.3, Tauris et al. (1999) deduced a companion mass of about $2\,M_{\odot}$ or less and a very extreme orbital eccentricity ($e \sim 0.9$). More recently, Jonker et al. (2007) determined that the companion is more massive, most likely an A0 to B5 type supergiant, and revised the orbital eccentricity to a more moderate value ($e \sim 0.45$), reviving an original identification by Whelan et al. (1977).

The picture definitely changed when Heinz et al. (2013) revealed a faint X-ray supernova remnant associated with Cir X-1. This allowed the determination of the age of the system as about 4500 yr, which has two important consequences, besides making Cir X-1 the youngest X-ray binary of its class known today. It implies that the neutron star should have a magnetic field exceeding 10^{12} Gauss (Kaspi 2010), which is at odds with the occasional observation of type I X-ray bursts in this source. Such events are usually observed in old, low-mass X-ray binaries with magnetic fields below 10^{9} Gauss and where the accretion stream is hardly affected by such a low field. Such youth also reaffirms the determination that the companion is massive, because a low-mass star could not have had time to evolve to fill its Roche lobe at periastron. In a core collapse, the progenitor star was also massive (Jonker et al. 2007); the companion star should then be a massive main-sequence star that is a few tens of megayears old. Once the binary orbit is largely circularized, Cir X-1 will eventually become a high-mass X-ray binary as we know them today. The possibility that the supernova was caused by an accretion-induced collapse (AIC; Bhattacharya & van den Heuvel 1991) is unlikely because neutron stars in electron-capture supernovae are not expected to receive a significant kick and is inconsistent with the dynamic orbital parameters and evolution of the system (Clarkson et al. 2004; Heinz et al. 2013; Tauris et al. 2013).

In X-rays, Cir X-1 exhibits two main variability patterns: one happens on short timescales related to its orbital period, and another spans many years with X-ray fluxes changing from mCrab levels to several Crab. One orbit lasts about 16.5 days (Kaluzienski et al. 1976), and for most of its orbital tenure, X-ray emissions are fairly persistent. Due to its orbital eccentricity, the neutron star and its accretion disk actually spend most of the time detached from the companion star. Near zero phase (periastron), the Roche lobe of the companion

Table 1
Chandra X-Ray Observations

Chandra ObsID	Obs. ID	Start Date (UT)	Start Time (UT)	Exposure (ks)	Phase ⋯	HETG First Rate (cts s^{-1})
8993	V	2008 July 16	07:57:55	32.7	Periastron	0.12
12235	VI	2010 July 4	05:04:05	19.4	Apastron	1.13
18990	VIIa	2017 June 6	12:35:21	13.2	Periastron	0.14
20093	VIIb	2017 June 6	22:00:54	9.8	Periastron	0.15
20094	VIIc	2017 July 7	06:50:07	35.3	Periastron	0.22

overflows and the neutron star/disk system attaches to the overflow stream and actively accretes matter. This results in a significant rise in X-rays at periastron passage, which at times can radiate up to super-Eddington fluxes (Brandt et al. 1996; Brandt & Schulz 2000; Schulz & Brandt 2002). The frequency and strengths of these periastron flares also seem to follow a long-term variability pattern that spans 30 yr (Parkinson et al. 2003).

This long-term light curve reflects the flux changes of 30 yr measured with most of the major detectors and observatories available up to 2001. In the mid-1990s, Cir X-1 was as bright as 2 Crab and exhibited relativistic radio jets (Stewart et al. 1993; Fender et al. 1998). ASCA observations showed that the accretion disk is probably viewed fairly edge-on (Brandt et al. 1996). One of the biggest revelations was delivered by the first *Chandra X-ray Observatory* observations, which showed strong P Cygni lines, indicating a powerful and variable accretion disk wind (Brandt & Schulz 2000; Schulz & Brandt 2002). Heinz et al. (2007) discovered a parsec-scale X-ray jet (see also Sell et al. 2010), manifesting the picture that at times of high flux Cir X-1 behaves like a true microquasar (Mirabel 2001). Since then, the X-ray source has dimmed steadily. In 2005, the source was already down in flux by more than an order of magnitude. While the P Cygni lines were gone, an emission line spectrum emerged rich in H- and He-like lines from high-Z elements such as Si, S, Ar, Ca, and Fe at very high neutral columns. There was a notable presence of an ionized absorber, as well as some resonant absorptions, indicating a rather weak disk wind. Since these observations, the X-ray flux continued to drop into levels below 10 mCrab. In a rare event, the X-ray source at periastron experienced a larger outburst in 2010, during which Cir X-1 exhibited type I X-ray bursts (Linares et al. 2010; Papitto et al. 2010). This period was extensively covered with *RXTE* and one *Chandra* observation, providing much temporal and spectral information but no definite conclusions with respect to the origins of the X-ray continuum (D'Aì et al. 2012). However, it confirmed that Cir X-1 is a neutron star X-ray binary.

In this paper, we analyze a series of observations between 2008 and 2017 that were taken at the absolute lowest flux levels in decades with the goal of characterizing the nature of the X-ray source at these levels, as well as finding interfaces to the newly evolving picture that Cir X-1 is a very young, massive main-sequence X-ray binary.

2. *Chandra* Observations

Cir X-1 was observed with the high-energy transmission grating spectrometer (HETGS; see Canizares et al. 2005 for a detailed description) once in 2008 and a few times in 2017. Table 1 summarizes all its parameters. The 2008 observation we denominate as "V" and the 2017 observations as "VIIa-c." We add one more observation done in 2010 (PI: D'Ai) and label this one as "VI." This is in line with the denominations defined in Schulz et al. (2008) in sequence with the previous *Chandra* HETGS observations. Observations I and II are described in Brandt & Schulz (2000) and Schulz & Brandt (2002), and observations III and IV in Schulz et al. (2008). Observations V and VIIa-c were all performed during periastron passage, and observation VI was done at apastron passage.

All observations were reprocessed using CIAO 4.9 using CIAO CALDBv4.7.7 products. Updates to CIAO and its products since then did not impact the analysis preformed at the time of submission. The wavelength scale was determined by measuring the zero-order position to a positional accuracy of about half a detector pixel, ensuring a wavelength scale accuracy of about a quarter resolution element, that is, 0.005 Å for medium-energy grating (MEG) and 0.003 Å for high-energy grating (HEG) spectra. For our previous observations, we could not use a direct zero-order source detection because the point-spread function of the source was too piled up. In that case, we measured the zero position by determining the intersection between the readout streak and the grating dispersion arms. In this analysis, we applied both methods, and their results agreed well within the accuracy stated above. Note in observation III (Iaria et al. 2008; Schulz et al. 2008) that we did not even have a source readout streak, which introduced a systematic uncertainty that resulted in slight redshifts in the detected lines. It is thus paramount that we maintain a high confidence in the location of the zero-order position. For transmission gratings, the dispersion scale is linear in wavelength, so we perform all analyses in wavelength space. This ensures the most accurate scales through multiple binnings. We used standard wavelength redistribution matrix files but generated ancillary response files (ARFs) using the provided aspect solutions, bad pixel maps, and CCD window filters.[7] For all the observations, we generated spectra and analysis products for the MEG $+1$ and -1 orders, as well as for the HEG $+1$ and -1 orders. Figure 1 shows coadded first-order HETG spectra for all periastron observations (V and VIIa-c) binned by a factor 4, which represents about one MEG resolution element per spectral bin. The light curves of the periastron observations are all very similar and flat without any structure, and we therefore do not present any plots. Observation V is very faint with 0.12 c s^{-1}, VIIa and b are similar, and observation VIIc is slightly brighter (see Table 1). The apastron observation (VI) was taken during a specifically strong outburst and is an order of magnitude brighter than all the other observations. This observation is shown in Figure 2.

[7] See http://asc.harvard.edu/ciao/threads/.

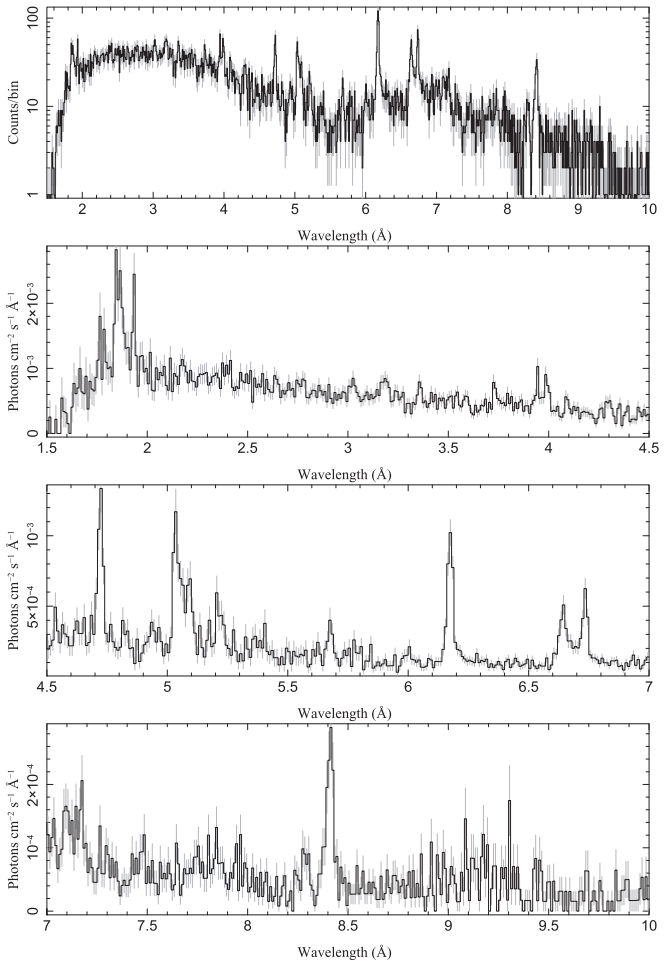

Figure 1. Raw-count HETG first-order spectrum of the coadded observations (top panel). A more spread-out, unfolded spectrum of the HETG first order (bottom three panels) for V and VIIa-c.

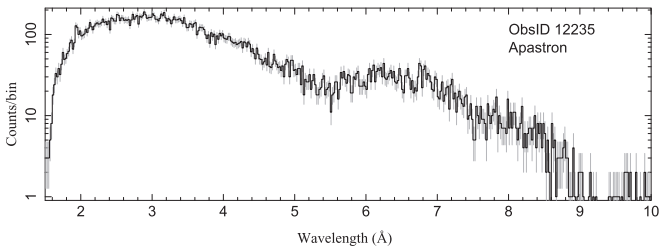

Figure 2. X-ray spectrum at apastron during an intermediate outburst in 2010.

3. Spectral Analysis

For the spectral analysis, we focus exclusively on the four periastron observations. Each individual observation does not have enough statistics to perform a detailed line analysis, and in general we coadd all of them in the plotting and fit them simultaneously in the analysis. Because these observations were over an order of magnitude fainter than the ones in Schulz et al. (2008), we used a *Cash* statistic (Cash 1979) for the fits. This only reflects a more accurate treatment of low statistics data while still allowing for a consistent comparison with previous much brighter observations.

Figure 1 shows faint and bright lines in the spectrum. To determine the continuum, we remove these wavelength regions from the spectral model fit. The observed lines all appear at known line wavelengths for Mg, Si, S, Ar, Ca, and Fe, and they also appear quite narrow. We removed 0.05 Å regions around the detected line centroids for the line centroids (see Section 3.2) detected for these elements. All spectra then have 1011 data bins in the unbinned case. We do not bin the spectra during the fits as this introduces statistical biases. However, we do match the grids of the HEG to the MEG spectra to plot the combined spectrum.

3.1. X-Ray Line Analysis

The coadded spectrum in Figure 1 shows very strong H- and He-like lines for Mg, Si, and S with line counts between 150 and 320 cts line^{-1}. This is large enough to allow the determination of critical line parameters such as line shifts, widths, and flux. For this analysis we use Gaussian line functions. The H-like lines and the Fe K line are single Gaussians. We do not account for the spin–orbit split in the H-like lines, which produces a separation of the α_1 and α_2 lines by 0.0056 Å, and we use the average line location as was done in Schulz & Brandt (2002) and Schulz et al. (2008). This allows us to better compare the line measurements. As a consequence, we may slightly overestimate the line width in H-like lines. The He-like lines are triplets containing a resonance (r), an intercombination (i), and a forbidden (f) line with fixed line spacings. Here we froze the line spacings of the i and f lines relative to the r lines. We then divided the bandpass into five regions containing the Mg, Si, S, Ca + Ar, and Fe lines.

3.1.1. Line Fluxes

The results of the line fits to the periastron data in Table 1 are shown in Table 2. The first column lists the K-shell ion, the second column gives the theoretical line location as in Schulz et al. (2008), the third column is the measured wavelengths, the fourth column gives line fluxes in units of 10^{-5} photons s^{-1} cm^{-2}, and the fifth column lists the sigma of line widths in km s^{-1} ($3\times10^5(\sigma_{\rm meas}/\lambda_{\rm meas})$). There are distinct differences in the line fluxes with respect to previous observations when the source was brighter. Figure 3 shows that the bulk of the H-like line fluxes were of the order of 20% of the ones reported in Schulz et al. (2008), while the He-like lines are up to 70% of the previously reported fluxes. Calcium lines are the exception as they were generally weak in observations III and IV (Schulz et al. 2008). The lines in the Fe K line region follow this picture: the H-like Fe XXVI is very weak and the region is dominated by the Fe XXV triplet. However, the Fe K line (Fe I–X) is very similar in flux and width to the one we observed in observation III. The line widths cluster around 550 km s^{-1}, which is very similar to previous detections. The line widths at shorter wavelengths appear higher, which is likely a consequence of the increasingly lower spectral resolution at shorter wavelengths. The size of an HETG resolution element of a dispersed grating order is constant in wavelength space, and thus resolution element sizes increase in velocity toward higher energies.

3.1.2. Line Centroids

Figure 4 shows the line centroids with the expected rest positions in units of km s^{-1}. The filled black circles show the periastron observations from Table 1. The majority of the brightest lines concerning Mg, Si, and S clearly show a

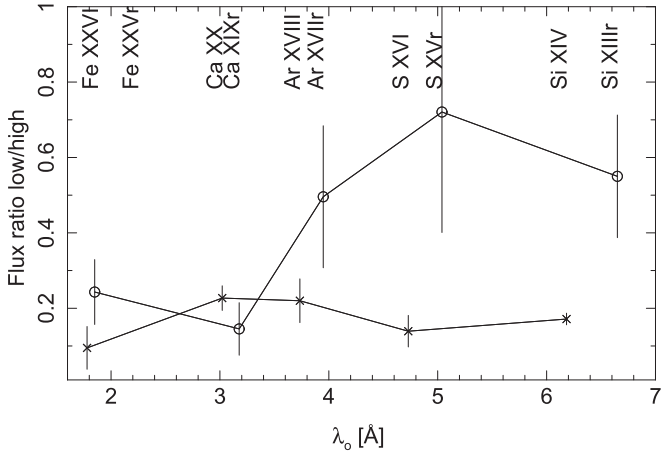

Figure 3. Line ratios of the H- and He-like resonance lines from the high-flux observations in Schulz et al. (2008) and the low-flux observations reported in this paper.

Table 2
X-Ray Line Properties from the Periastron Observations in Table 1

Ion	λ_o(1) (Å)	λ_{maes} (Å)	Line Flux (10^{-5} ph s^{-1} cm^{-2})	σ (km s^{-1})
Fe XXVI	1.780	1.782 ± 0.010	0.92 ± 0.99	<3300
Fe XXVr	1.850	1.845 ± 0.008	3.84 ± 2.23	1000 ± 820
Fe XXVi	1.859	1.858 ± 0.008	0.10 ± 8,38	1000 ± 820
Fe XXVf	1.868	1.870 ± 0.005	3.25 ± 3.60	1000 ± 820
Fe K	1.940	1.933 ± 0.001	2.49 ± 0.85	390 ± 430
Ca XX $L\alpha$	3.021	3.021 ± 0.008	0.59 ± 0.44	770 ± 640
Ca XIXr	3.177	3.171 ± 0.007	0.30 ± 0.36	750 ± 510
Ca XIXi	3.189	3.183 ± 0.007	0.74 ± 0.55	750 ± 510
Ca XIXf	3.211	3.205 ± 0.007	< 0.1	750 ± 510
Ar XVIII $L\alpha$	3.734	3.736 ± 0.003	0.88 ± 0.35	500 ± 460
Ar XVIIr	3.949	3.946 ± 0.004	1.19 ± 0.39	600 ± 310
Ar XVIIi	3.966	3.963 ± 0.004	0.14 ± 0.50	600 ± 310
Ar XVIIf	3.994	3.991 ± 0.004	1.32 ± 0.49	600 ± 310
S XVI $L\alpha$	4.730	4.722 ± 0.002	2.95 ± 0.55	450 ± 140
S XVr	5.039	5.036 ± 0.003	2.45 ± 0.54	470 ± 130
S XVi	5.067	5.064 ± 0.006	0.97 ± 0.44	470 ± 130
S XVf	5.102	5.093 ± 0.003	1.32 ± 0.43	470 ± 130
Si XIV $L\alpha$	6.183	6.175 ± 0.001	2.64 ± 0.28	420 ± 70
Si XIIIr	6.650	6.640 ± 0.003	1.32 ± 0.24	500 ± 80
Si XIIIi	6.669	6.678 ± 0.003	0.63 ± 0.34	500 ± 80
Si XIIIf	6.740	6.734 ± 0.002	1.40 ± 0.24	500 ± 80
Mg XII $L\alpha$	8.422	8.409 ± 0.004	0.94 ± 0.18	530 ± 140
Mg XI(r)	9.169	9.179 ± 0.015	0.25 ± 0.14	< 480
Mg XI(i)	9.230	9.228 ± 0.012	< 0.1	< 480
Mg XI(f)	9.314	9.315 ± 0.013	0.22 ± 0.15	< 480

Note. (1) See Schulz et al. (2008).

line shift to the blue of about 400 km s^{-1}. Higher Z element lines (Ar, Ca, and Fe) are fainter and uncertainties are larger.

For comparison, we plot the results from observation IV from Schulz et al. (2008) for reference (squares). For this observation, we had to refit the He-like triplets (Fe, Ca, Ar, S, and Si) because in that previous analysis the widths and line spacings were free parameters and not tied according to their triplet properties. In some cases, specifically for the Si, Ar, and Ca triplets, this produced line centroids that are much more consistent with the rest of the sample. The line centroids from observation IV are consistent with the expected rest wavelengths.

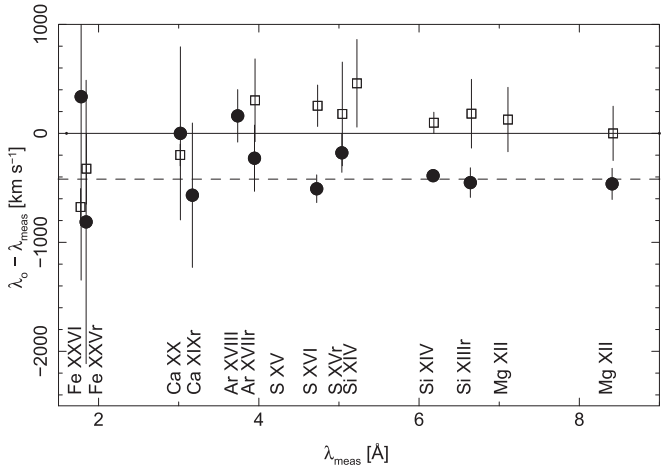

Figure 4. Measured line centroids with respect to theoretical values in velocity units. Negative values are blueshifts. The straight line is zero velocities from the theoretical line values. The dashed line marks the average blueshift of −410 km s^{-1} seen in the periastron observations V and VIa-c. The squares are the data from Schulz et al. (2008) for observation IV for reference.

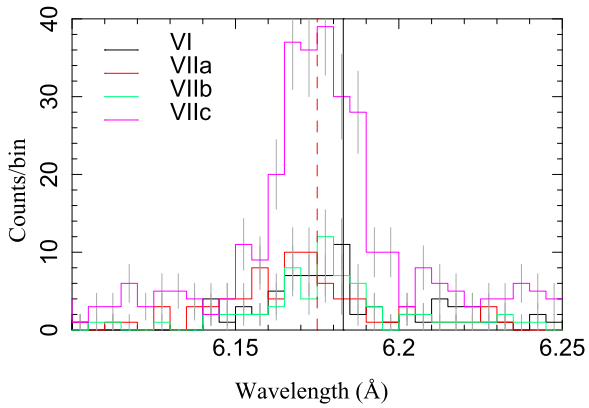

Figure 5. Si XIV L_α line for all four observations plotted separately. The dashed line marks the centroid location of the coadded line fits. The solid line marks the rest wavelength location. It shows that all observations agree with a line centroid location blueshifted by about 400 km s^{-1}.

The Si XIV L_α at the expected wavelengths is by far the most significant one in terms of total counts (>300 cts), and here we can look at the individual observations. The brightest contribution comes from observation VIIc (∼170 cts) and the faintest from observation V (∼35 cts), enough to allow centroid studies. Figure 5 shows the line counts of the unbinned data. The black line marks the expected rest wavelength at 6.183 Å, and the dashed line gives the fitted location of the coadded line data. It clearly shows that the blueshift is present in all observation segments and appears persistent over many years. The lines of observations V and VIIa,b are symmetric around the fitted centroid (dashed line).

3.1.3. G and R Ratios

Line flux ratios are a powerful tool for diagnosing detailed properties of an ionized gas (Bautista & Kallman 2000; Porquet & Dubau 2000). A gas at temperatures of <1 MK that is photoionized is expected to emit lines primarily by recombination cascades and will have G-line flux ratios of $G = (f + i)/r > 4$ or close to that value for atomic numbers Z of 12 and higher. From the fluxes in Table 2 we find G values of 1.53 ± 0.30, 0.93 ± 0.60, 1.22 ± 0.49, 2.46 ± 1.11, and

0.87 ± 1.07 for Si, S, Ar, Ca, and Fe, respectively. These values appear well below the expectation for a pure photoionized plasma, indicating some form of hybrid plasma. We rule out EUV photoexcitation as this would depopulate the α resonance line and produce higher-order transitions that do not appear in Table 2. Two processes can lead to enhanced resonance line emissions: one is collisional ionization in very hot plasmas, and the other is resonance scattering. We can rule out contributions from a collisionally ionized plasma as here the excitation of K-shell ions with atomic number larger than 14 would also require temperatures in excess of 10 MK and the presence of a significant bremsstrahlung continuum, which we do not observe. What we observe is likely photoionized plasma affected by resonance scattering. In that case, the presence of a medium with high optical depth can scatter resonance line fluxes unisotropically into preferential directions depending on geometry. Modeling of this effect requires extensive knowledge of the geometry and local plasma properties.

Gas densities can be diagnosed with the $R = f/i$ ratio for which we expect that, at $R > 1$, densities are below a critical density for a specific atomic number Z. Our sample features He-like triplets for Si, S, Ar, Ca, and Fe and features critical densities of $\sim 10^{14}$, $\sim 10^{14}$, $\sim 10^{15}$, $\sim 10^{16}$, and $\sim 10^{17}\,\mathrm{cm}^{-3}$. In all cases, we find R values much larger than unity except for Ca, where we only detect an upper limit for the f line. This points to plasma densities lower than $\sim 5 \times 10^{14}\,\mathrm{cm}^{-3}$ assuming an isotropically mixed gas. The R ratio is also very susceptible to UV radiation where the metastable forbidden line levels get depopulated into intercombination line levels. That the f lines in Table 2 generally appear stronger than the corresponding i lines shows that effects from UV radiation appear not to be significant.

The lines in the Fe K line region follow this picture: the H-like Fe XXVI is very weak and the region is dominated by the Fe XXV triplet. However, the Fe K line (Fe I–X) is very similar in flux and width to the one we found in observation III.

3.2. Photoionization Modeling

Figure 1 features strong He-like lines with especially strong r lines. The ionization parameter is defined as

$$\xi = L_x/(nd^2), \quad (1)$$

where L_x is the source luminosity, n the plasma density, and d the distance from the X-ray source. A multiple plasma environment requires a range of ionization parameters to engage in a fit. This complicates the modeling process in terms of fitting time and parameter range. In that light, we try to limit the number of fit components to a very minimum. For the choice of continuum, we modeled a few cases including combinations of power laws as reported by Schulz et al. (2008) and Iaria et al. (2008), as well as blackbody spectra. For the fit itself, we use *XSTAR*'s *photemis* function available in *Xspec*, which allows for a preset atomic-level population file to calculate a photoionized spectrum for a single ionization parameter. For the final fit setup, we used two different functions to account for two ionization parameters. Furthermore, in order to be able to fit the H- and He-like line morphology, the functions also needed individual absorption columns, for which we applied *pcfabs* functions. For the fits, we fixed the interstellar column to $1.8 \times 10^{22}\,\mathrm{cm}^{-2}$ as reported by Heinz et al. (2013). The fits generally converged to a one-component solution for the continuum, that is, either a power-law or a blackbody spectrum. The power-law solution was ruled out because it completely overshot the observed continuum above 2 Å for the Fe K line region, whereas the 1.6 keV blackbody provided the necessary steep decline above 2 Å (see Figure 6). The fit result is summarized in Table 3. The uncertainties are 90% confidence limits calculated by *conf_loop* in *ISIS*. In the fit, we also set the turbulent velocities to $600\,\mathrm{km\,s}^{-1}$, and in the final stages we fixed some of the abundances we let float. The redshifts were also fixed to $-400\,\mathrm{km\,s}^{-1}$ (see dashed line in Figure 4) in one of the *photemis* components and allowed to float in the second. We need at least two ionization parameters because we observe Mg and Si lines as well as Ca and Fe lines, which cannot be modeled with a single ionization parameter (Kallman et al. 2004). The Mg abundance was slightly reduced to 0.93, which likely is a consequence of the statistically challenging Mg XI

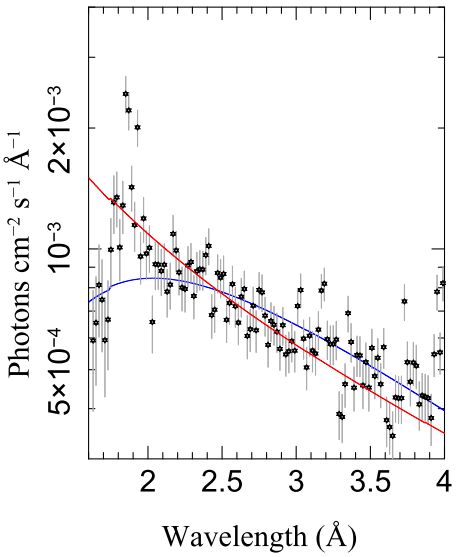

Figure 6. Comparison of the power-law fit (red) to the blackbody fit (blue) in the Fe K line region (the data are black).

Table 3
Photoionization Fit Results

Parameter	Symbol	Units	
Absorption column density	$N_{\rm H}$	$10^{22}\,\mathrm{cm}^{-2}$	1.8
Blackbody temperature	kT	keV	1.57 ± 0.04
Blackbody normalization	$(R_{\rm km}/D_{\rm 10kpc})^2$	⋯	0.392 ± 0.026
Pcf absorption column 1	$N_{\rm H}^1$	$10^{22}\,\mathrm{cm}^{-2}$	2.4 ± 0.4
Photoionization normalization 1	K_1	erg cm^{-1} s^{-1}	121.5 ± 12.7
Ionization parameter 1	ξ_1	erg cm s^{-1}	340 ± 135
Redshift 1	z_1	⋯	−0.0013334
Pcf absorption column 2	$N_{\rm H}^2$	$10^{22}\,\mathrm{cm}^{-2}$	2.8 ± 1.1
Photoionization normalization 2	K_2	erg cm^{-1} s^{-1}	100 ± 65
Ionization parameter 2	ξ_2	erg cm s^{-1}	1500 ± 180
Redshift 2	z_2	⋯	−0.00062
Fit statistic	Cash/dof	⋯	1.42

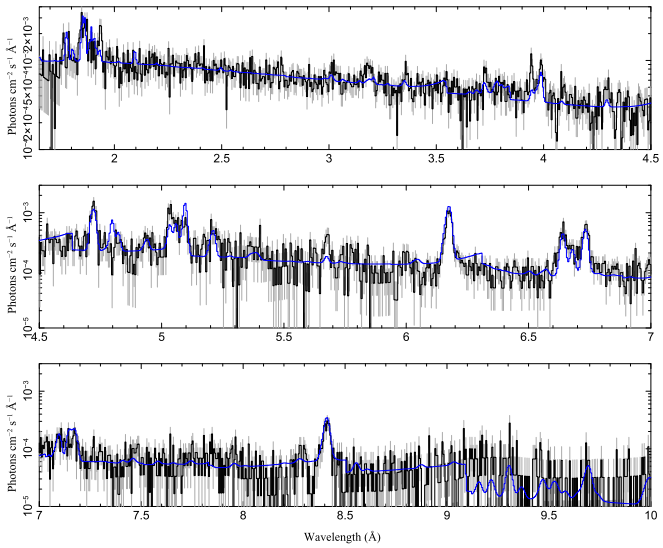

Figure 7. Photoionization model fit using the *XSTAR:photemis* function.

bandpass. The Si abundance was set to 1.73 and the S abundance to 1.68 for both *photemis* components.

The photoionization model fit result is shown in Figure 7. The final ionization parameters obtained were $\xi = 340$ and 1500 erg cm s^{-1}, and both are associated with high column densities. The covering fractions were free parameters but resulted in 0.99 in both cases. The plasma with ionization parameter 340 erg cm s^{-1} is responsible for the bulk of the line fluxes, while the one with ionization parameter 1500 erg cm s^{-1} contributes to some of the H-like line fluxes but mostly to the Fe region.

The normalization of the photoionization model is defined by

$$K = \frac{\mathrm{EM}}{4\pi D^2} \times 10^{-10}, \quad (2)$$

where EM is the emission measure of the gas in units of cm^{-3} at the involved ionization parameter, and D is the distance to Cir X-1 in units of cm. For a distance of 9.4 kpc (Heinz et al. 2015), this leads to

$$\mathrm{EM} = K \times 1.06 \times 10^{56}. \quad (3)$$

For the plasma with log $\xi_1 = 340$ erg cm s^{-1}, we obtain $\mathrm{EM}_1 = 1.3 \times 10^{58}$ cm^{-3}, and for log ξ_2=1500 erg cm s^{-1} we obtain $\mathrm{EM}_2 = 1.1 \times 10^{57}$ cm^{-3}. These emission measures are only slightly smaller than the one estimated by Schulz et al. (2008); the observed source luminosity, however, appears to be significantly lower.

This observed low X-ray luminosity from the continuum is inconsistent with the observed photoionized luminosity from the X-ray line analysis. One of the difficulties is maintaining the observed ionization parameters at such a low luminosity over such a large volume. While to some extent one could offset a larger source distance d with a lower density in the wind n, this eventually breaks down because the observed photoionized luminosity appears close to the actual source luminosity. Such a high ionization efficiency is nearly impossible to achieve under likely any circumstances. This points in the direction that part of the X-ray source is still obscured, something we encountered during the analysis of observations I and II (Schulz et al. 2008). To simply assume

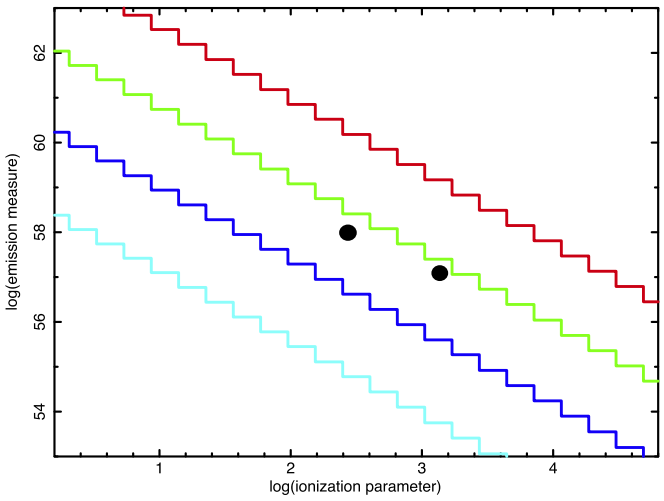

Figure 8. Calculation of emission measure in dependence on ionization parameter for a static corona as done in Schulz et al. (2008). The color lines are for various luminosities: log L_x = 38 (red), 37 (green), 36 (blue), and 35 (light blue) in units of erg s^{-1}. The two black circles are the results from the photoionization modeling.

that some of the flux of our observed continuum is partially blocked and should be higher is possible but not a good solution because a 1.6 keV blackbody is inherently inefficient at ionizing high-Z atoms such as Fe and Ca at any possible luminosity. A more promising scenario relates back to our actual findings in Schulz et al. (2008). There we found that the observed photoionized lines are due to an accretion disk corona (ADC), and in order to sustain such a corona, the source X-ray luminosity needed to be significantly higher than observed, which leads to the conclusion that parts of the central X-ray source are obscured. This may still be the case. Figure 8 shows a recalculation of the content of Figure 5 in Schulz et al. (2008), including lower luminosity predictions and the locations of our photoionized data points in this picture. This indicates that for our results the source still is at a luminosity close to 10^{37} erg s^{-1}, which allows for sustaining a static ADC. This then leaves the possibility that we do observe some highly absorbed and obscured parts of the ADC in the high-Z lines and the photoionized wind of the companion seen in the blueshifted lower-Z lines.

The ionization parameter and emission measures then leave us with a wide range of viable plasma regimes. Two regimes that are opposite in character are of interest in the case of Cir X-1. One refers to the ADC emissions as described in Schulz et al. (2008), which are confined to the domain of the accretion disk. In that case, we can assume that d, the distance to the X-ray source, is of the same order of magnitude as r, the size scale of the photoemitting region. For distances of up to 10^{10} to 10^{11} cm from the neutron star surface, we obtain ADC plasma densities between about 10^{12} and 10^{14} g cm^{-3} in a compact volume within the accretion disk (see also Jimenez-Garate et al. 2002).

The observed blueshifts point to another regime. For very low densities as exist in weak stellar winds, that is, densities g cm^{-3}, we also get viable solutions for values of d and r that are beyond the dimensions of the accretion disk. Weak, low-density winds are expected in mid-B-type stars. For such low plasma densities, the dimensional parameters are larger than 10^{12} cm, consistent with ionized line emissions in a weak stellar wind.

The *XSTAR:photemis* function applies a model describing a purely photoionized plasma. The fact that this model cannot properly account for the strength of the resonance lines in some of the He-like triplets confirms our findings from the *G* ratios that there is a significant contribution from some recombination and resonance scattering. Future modeling of these effects should reveal the presence of such a scattering medium.

4. Discussion

The X-ray source in the Cir X-1 binary has given us many different looks in the past in terms of variability, flux, and spectral properties. Since the first *Chandra* HETG observation in the year 2000, where the source flux still exceeded 1.5 Crab, the X-ray source has dimmed by more than three orders of magnitude until it went below one mCrab in 2009 (see Figure 3 in Heinz et al. 2013). Its spectral continuum shape similarly has morphed from two partially covered blackbodies during its high state (Brandt et al. 1996; Schulz & Brandt 2002), to two or one partially covered power laws (Iaria et al. 2008; Schulz et al. 2008), and now to a single blackbody with just interstellar absorption. Besides exhibiting various levels of line emission and absorption, there always was the presence of enormous levels of either partially covered cold or warm intrinsic continuum absorption. High levels of source intrinsic absorption are also present in the observations we report in this paper, except in these new observations these absorbers have only little effect on the continuum and mostly affect the photoionized regions. This is an aspect we have not seen before, and it appears to be fundamentally different from the previous observations.

4.1. Origin of the X-Ray Continuum in This Very Low State

The final continuum spectrum in the photoionization fit turned out to be a 1.6 keV blackbody. We had fixed the interstellar column to $1.8 \times 10^{22}\,\mathrm{cm}^{-2}$, which was found by Heinz et al. (2013) in the fit to the supernova remnant, consistent with the large amount of visible extinction toward Cir X-1, as well as a well-established distance of 9.4 kpc (Heinz et al. 2015). Such a distance is also consistent with Cir X-1 radiating at Eddington peak fluxes when it was brightest (Jonker & Nelemans 2004) and when it exhibited P Cygni X-ray lines from a radiation-driven wind (Brandt & Schulz 2000). The property of the blackbody fit is rather peculiar as it exhibits a very small emission radius. It is also notable that there is no or only very little contribution of the accretion disk to the observed X-ray spectrum. The only clear signature from the disk may come from the Fe K fluorescence line observed at 1.93 Å.

The big problem arises when we realize that our observed continuum is quite insufficient to photoionize the plasma at the level observed. This gives us reason to assume that emissions from the accretion disk are there but are highly absorbed and obscured. This provides quite some uncertainty to the observed luminosity and nature of the X-ray spectral continuum as we have to consider that the bulk of the emission is partly blocked and obscured.

Accreting neutron stars with magnetic fields significantly lower than 10^{10} Gauss are generally seen in low-mass X-ray binaries (LMXBs), which are considered to be older systems in which the original field had enough time to decay to such low values. With only a very few exceptions where we do not know the field through cyclotron lines, accreting neutron stars with high-mass companions have all high magnetic fields as they are considered very young. However, we point out that the question of the companion nature is fairly irrelevant here. Homan et al. (2010) showed that transient sources can morph through atoll and *Z* stages at various flux phases, making these spectral variability imprints more related to effective Roche-lobe overflow accretion rather than binary types. In the following, we discuss how the observed continuum relates to cases of low and high magnetic fields for the accreting neutron star.

4.1.1. Low-field Case

One of the reasons why Cir X-1 used to be considered an LMXB was its spectral variation pattern during its brightest flux phases showing the nature of a *Z*-source. We then may compare it to a rare class of LMXB pulsars, such as the transient Terzan 5 (IGR J17480-2446) or the persistent ultracompact binary pulsar 4U1626-67. At an estimated magnetic field between 10^9 and 10^{10} G, Terzan 5 is much older, and its accretion stream is likely only weakly affected by the magnetic field. As a consequence, its spectral signatures are expected to be more comparable to neutron star atmospheres or normal LMXB emissions depending on whether the transient is in a subcritical or critical state (see Degenaar et al. 2013 and references therein). Pulsar 4U 1626-67 with a magnetic field of 4×10^{12} G (Orlandini et al. 1998) is much younger, but because its luminosity is persistently close to critical, its continuum emission relates more to what we observed in Cir X-1 during its intermediate flux phases (Schulz et al. 2008).

A significantly higher blackbody luminosity also significantly increases the emission radius to sizes that are more reminiscent of neutron stars with low magnetic fields in which the accretion flow is hardly affected by the magnetic field, and we can identify random hot patches or boundary layers on the neutron star surface as emission regions. Such blackbody continua are not particularly unusual in LMXBs; prime examples are 4U1626-67 (Schulz et al. 2001), 4U1822-37 (Ji et al. 2011), Her X-1 (Ji et al. 2009), or Aqu X-1 (Sakurai et al. 2014). However, in all of these cases that blackbody component exhibits temperatures of about 0.5 keV. High temperatures as observed here are more prominent in the peaks of type I X-ray bursts, and in fact the continuum temperature observed here is close to what Linares et al. (2010) report for the top temperatures observed in the 2010 X-ray bursts from Cir X-1. That is very unusual for LMXBs. The fact that this continuum is heavily absorbed and some of this absorption is unaccounted for changes little, as it is the part <2Å that defines the blackbody in the fit and its temperature. We note that neither Schulz et al. (2008) nor Iaria et al. (2008) observed a blackbody when the source was an order of magnitude brighter but report a more suitable power law for the observed photoionizations as the continuum. The shape of a 1.6 keV blackbody is not particularly suited for K-shell ionizations of high-*Z* atoms as its shape drops dramatically above 7 keV and lacks the harder photons. Should the neutron star have a low field as is common in LMXBs, then the observed continuum properties are quite unusual and hard to explain. It would also make Cir X-1 the youngest neutron star with a low magnetic field known to date.

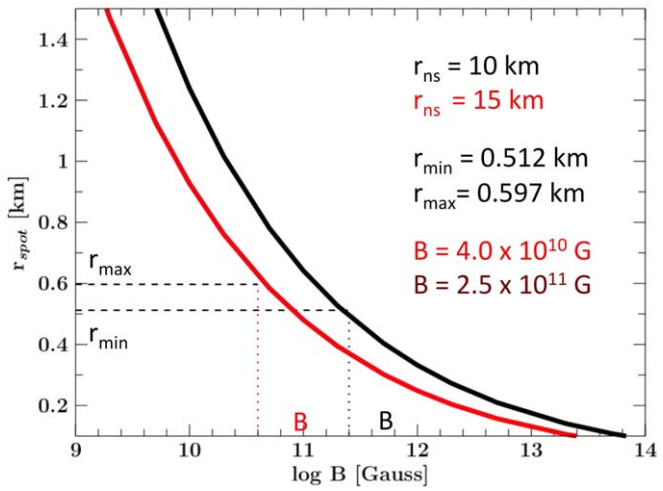

Figure 9. Evaluations of Equations (4) and (5) for a neutron star radius of 10 km (black) and 15 km (red). The limits $r_{\rm min}$ and $r_{\rm max}$ are derived from the blackbody fit results in Table 2 for a distance of 9.4 kpc.

4.1.2. High-field Case

However, what is very common is the fact that young neutron stars, accreting or isolated, have high ($\gg 10^{10}$ G) magnetic fields (Reig 2011; Özel & Freire 2016). In this case, we consider the possibility that this observed blackbody continuum does not contribute much to the photoionization process at all and the photoionizing continuum is entirely obscured. In a high-field accretion scenario, matter is predominantly funneled by the field onto poles of the neutron star, and the state of the accretion column depends on X-ray luminosity (see Becker & Wolff 2007 for an in-depth review). At a critical luminosity of $L_{\rm crit} = 1.5 \times 10^{37}$ erg s^{-1}, the accretion flow becomes radiation pressure dominated, and X-ray emissions are defined by a complex mix of physical processes, resulting in something close to a power law with an exponential cutoff or similar as observed when the source was brighter (Schulz et al. 2008). However, in the subcritical case where the luminosity is erg s^{-1}, as is observed in the low state of Cir X-1, the emissions from the bare hot spot can be explained by such a hard blackbody.

In such a subcritical environment, we can expect that the X-rays are produced by impact on or very close to the neutron star surface. If this is the accretion hot spot, its radius r_0 should fulfill the condition (Lamb et al. 1973)

$$r_0 < r_{\rm ns}\left[\frac{r_{\rm ns}}{r_A}\right]^{1/2}, \quad (4)$$

where $r_{\rm A}$ is the Alfvén radius given by Becker & Wolff (2007) as

$$r_{\rm A} = 2.6 \times 10^8 B^{4/7} r_{\rm ns}^{10/7} M_{\rm ns}^{1/7} L_x^{-2/7}, \quad (5)$$

where B is the magnetic field in units of 10^{12} G, $r_{\rm ns}$ is the neutron star radius in units of 10 km, $M_{\rm ns}$ is the neutron star mass in units of $M_\odot$, and the X-ray luminosity L_x is in units of 10^{37} erg s^{-1}. Figure 9 shows the evaluation of Equations (4) and (5) for two different neutron star radii, with 10 km (black) representing the lower end of most equations of state and 15 km (red) representing the higher end of most equations of state (Özel & Freire 2016). Equation (5) has only a weak dependence on neutron star mass, and here we used a canonical value of 1.4 $M_\odot$. For L_x we applied the measured X-ray luminosity in Table 2. For a distance of 9.4 kpc (Heinz et al. 2015), we can determine limits to the blackbody emission radius depending on the blackbody fits provided in Table 2. This then amounts to an $r_{\rm bb} = r_{\rm min} = 0.512$ km and an $r_{\rm bb} = r_{\rm max} = 0.597$ km. At a distance of 9.4 kpc, the observed emission radius in Table 3 is 0.589 ± 0.151 km, consistent with these values. A relativistic color correction would do little to the range of these values. From that we find a lower limit to the magnetic field strength of 4.0×10^{10} G for a 15 km radius and 2.8×10^{11} G for a 10 km radius. Note that these are only lower limits, and the actual field can still be higher than these values.

A survey of about 20 confirmed cyclotron line energies in high-mass X-ray binaries (HMXBs; Caballero & Wilms 2012) shows that all but one magnetic surface field strengths are above 10^{12} G, except for *Swift* J1626.6-5156 (DeCesar et al. 2009), which has a field slightly below 10^{12} G. The result in Figure 9 of course depends on distance, while a cyclotron line measurement does not (Coburn et al. 2006). However, we deem a distance of 9.4 kpc quite robust. In order to have both the 10 and 15 km solutions above 10^{12} G, the distance has to be below 6 kpc, which is implausible because of the amount of extinction along the line of sight, and it would take the X-ray luminosity in observations I and II (Brandt & Schulz 2000; Schulz & Brandt 2002) too far away from Eddington conditions to produce such a powerful disk wind. Higher distances do not change the result much unless they become unrealistically high. In order for the field values to drop below 10^{10} G, the blackbody radius has to be higher than 1 km and the source would reside outside the Milky Way. We therefore are confident that the surface magnetic field in Cir X-1 is somewhere between the values shown in Figure 9.

The moderately high $\gg 10^{10}$ G magnetic field should still be consistent with a young system even though it is generally assumed that neutron stars are born with $>10^{12}$ G (see Kaspi 2010 and references therein). The neutron star in Kes 79 (Halpern & Gotthelf 2010) with a magnetic field of only 3.1×10^{10} G is a good example for a younger neutron star with a moderate magnetic field (see also Shabaltas & Lai 2012). Other examples are PSR J1852 + 0040 and 1E1207.4-5209 (Halpern et al. 2007; Gotthelf & Halpern 2007), as well as PSR J0821-4300 in Puppis A (Gotthelf & Halpern 2009), even though these may not be quite as young as Cir X-1. Thus, young neutron stars with lower magnetic fields of the order of 10^{11} G, also sometimes dubbed "antimagnetars," are not unusual anymore.

The observation of type I X-ray thermonuclear bursts (Tennant et al. 1986; Linares et al. 2010) also implies a field of G (Fujimoto et al. 1981). However, this criteria is more based on the lack of observations of type I bursts in X-ray pulsars rather than having a solid theoretical basis other than the suppression of convective motions to allow runaway burning in magnetic fields of about 10^{12} G and higher (Gough & Tayler 1966; Bildsten 1995). Bildsten (1998) outlined the conditions for neutron star nuclear burning for the case of high mass accretion rates ($\dot{M} > 10^{10}\ M_\odot$ yr^{-1}). At these rates, unstable nuclear burning is more easily realized. The luminosity of Cir X-1 during its outburst in 2010 was still below the stable burning criterion, and here the magnetic field may have been high enough to confine the accreted matter to

the ignition pressure, but still low enough to allow convective motions. We therefore argue that in the case that the neutron star magnetic field in Cir X-1 is only moderately high, the two facts that the neutron star is very young and that we observe type I X-ray thermonuclear bursts are consistent with what we know today.

4.2. Nature of the Blueshifts

The most prominent difference in the observed line properties, besides the fact that the He-like resonance lines appear enhanced, is the blueshifts of about 400 km s^{-1} in most of the observed lines. In Schulz et al. (2008), the lines were at rest and identified as ADC emissions from the accretion disk. In this low state, blueshifted line emissions now need a two order of magnitude higher ionizing luminosity to sustain such an ADC in the accretion disk. The flux of the lines and the amount of blueshift in the lines appear small and may not have significantly affected the line profiles in observations III and IV specifically because the shifts are of the order of a grating spectral resolution element. However, we note that Iaria et al. (2008) claim a faint blue component in their line profile analysis in observation III. This could mean that this blueshifted emission is always present but gets overpowered by ADC emissions when the source gets brighter.

There is no viable explanation for blueshifted lines within the accretion disk, suggesting emission regions outside the disk. While Iaria et al. (2008) proposed possible jet emissions, the determined ionization parameters as well as emission measures and the amount of the blueshift are also consistent with X-ray illumination of a massive companion wind. A wind velocity of 400 km s^{-1} would point in the direction of a B5Ia supergiant (Prinja & Massa 1998) as a companion, confirming the identification from Jonker et al. (2007). There is not much room for later types because in this spectral type range terminal wind velocities decline rapidly with spectral type. We point out that B5 stellar winds themselves cannot produce X-rays through inner wind shocks, as we observe in more massive stars. In this case, the very-low-density outer terminal velocity zone of the wind gets illuminated by the X-ray source in Cir X-1. That we may observe the illumination of the stellar wind is also supported by an apastron observation taken during a more prominent outburst in 2010. Figure 2 shows a dominant continuum but no photoionized lines, which should have been detectable. Even with the brighter continuum, the three brightest lines in the periastron spectrum should still be detectable above a 5σ level. Yet the only line detected is the Fe K fluorescence line, which we commonly associate with the accretion disk. The absence of unshifted ADC lines at least with regards to S, Si, and Mg from the accretion disk is peculiar because if it is true that the X-ray emissions have not changed in luminosity and are further obscured than what we observed in observations III and IV, then these lines should still be there unless they are now also suppressed by heavy absorption. In that case, the photoionized emission from the stellar wind is all that is left for the observer, as well as some weak higher Z lines from the ADC.

The amount of the shift would also rule out much later types because terminal wind velocities decline rapidly with type (Lamers et al. 1995; Prinja & Massa 1998). Observations V and VIIa-c were taken between orbital phase 0.00 and 0.07 using the *RXTE*/ASM ephemeris (MJD = 50,082.04) and an orbital period of 16.54694 days from Shirey et al. (1998; see also Clarkson et al. 2004) for which the neutron star always illuminates the face of the star into a wind coming toward the observer, hence the blueshift. However, we point out that 400 km s^{-1} is also near the known rotational velocities of any Be-star in an X-ray binary (Reig 2011). So if it is not the wind but the stellar surface that gets ionized, then we should see blueshifts and redshifts depending on whether the compact object comes toward the companion or moves away and none when the compact object is a zero phase. With all the distractions from disk emissions in the previous observations gone, we believe that this is the first time we might see the companion wind itself.

For this one can estimate the contribution of a spherical B-star wind with a constant velocity and a specific mass loss rate to the emission measure by integrating over the available volume from a B-star radius of 10^{12} cm to infinity. With a spherical mass loss rate of $10^{-8}\,M_{\odot}$ yr^{-1} and a terminal wind velocity of 500 km s^{-1}, this results in emission measures of the order of 10^{55} erg cm^{-3} s^{-1}, which is only a fraction of what we observe. Increased emission measures require increased mass loss rates as well as nonspherical geometries. This indicates that if this is indeed the companion wind, it has to be enhanced. One indicator that this is the case could be the existence of significant amounts of resonance scattering in the He-like lines.

4.3. On the Possible High-mass Nature of the X-Ray Binary

The photoionized plasma requires a substantial absorber in the line of sight in addition to absorption from the interstellar medium (ISM). If the wind is indeed the emission line region, this absorber has to be able to cover the bulk of the stellar wind. Normal B5 supergiants are not well known to carry wind-produced stellar disks. The only plausible protagonists we know today are magnetic stars and Be-stars, in the latter case also mostly much earlier type B-stars. In both cases, a decretion disk fed by equatorial wind can be produced under various critical circumstances. In the case of Be stars, it may be a stellar rotation rate of more than 75% of the critical rate (see Rivinius et al. 2013 for a full review), while in the case of magnetic stars it is a strong magnetic field configuration confining the wind (see Gagné et al. 2005). Such disks can provide not only the additional line-of-sight absorber but also account for the resonance scattering we observe.

However, while this is still a lot of speculation, we can in the following consider what is observationally known for the case of Be-stars. Be-star X-ray binaries (BeXBs) are a sizable subgroup in the category of HMXBs. Perhaps the most famous in the class of BeXBs is GX 301-2. This system consists of an accreting magnetized neutron star in an eccentric orbit ($e \sim 0.46$; Sato et al. 1986; Koh et al. 1997). This is a very similar system except its orbit is three times as long and periastron passages are not as violent as in Cir X-1. Its optical counterpart is a B1.5Ia supergiant with a lower mass limit of $39\,M_{\odot}$, which is much larger than what is considered for Cir X-1, and here the Roche-lobe overflow connection never breaks (Sato et al. 1986; Watanabe et al. 2003; Kaper et al. 2006). However, there are many similarities, such as an inclination larger than 44°, which does not produce an eclipse but just barely misses the face of the star, producing dips in the light curve by the dense stellar wind. Jonker et al. (2007) also concluded, even though the inclination is high (Brandt et al. 1996), that in the case of Cir X-1 the neutron star never crosses the star (see also Iaria et al. 2008). The X-ray spectrum in

observation III (Schulz et al. 2008) is very similar to the one observed in GX 301-2, where the region above 5 Å is dominated by line emissions from the ionized wind and the region below is dominated by accretion disk activity (Sato et al. 1986; Koh et al. 1997; Watanabe et al. 2003; Fürst et al. 2011).

In Be-stars the regions above and below the disk are more or less equivalent to those surrounding normal B-stars (Rivinius et al. 2013). Fast rotation may even enhance the wind toward the polar regions (Puls et al. 2008). The fact that the companion in Cir X-1 is a supergiant does not make much of a difference. Most massive stars begin the main sequence as fast rotators and usually stay that way (Langer et al. 1997); during the supergiant phase, the star may see a reduction in the rotation rate due to the increasing stellar radius (Puls et al. 2008). Generally, there is no reason why a fast rotator would not retain its disk in the supergiant phase, and the case could be made that Cir X-1 might as well be the youngest known BeXB.

All BeXBs classified so far have orbital periods of 20 days and higher up to 300 days (see Reig 2011 for a review), and Cir X-1 with 16.5 days would mark the shortest period, which seems adequate since it would be the youngest in the sample. However, the list of known OBe stars mostly shows dwarfs (class V), subgiants (class IV), or giants (class III), and Cir X-1 would be the only other supergiant case (classes I and II) to GX 301-2. Supergiant X-ray binaries (SGXBs) tend to have shorter periods, and here Cir X-1 would have the longest of this class. It is also the case that almost all BeXBs show X-ray pulsations ranging from a few seconds to a few hundreds of seconds. To date, no pulsations have been reported for Cir X-1, and we also did not detect any in the range where we are sensitive, which is also above a few seconds. For the neutron star being that young, we should also expect much shorter periods, likely down to a few milliseconds. The lower magnetic field of 10^{11} G should not brake its period as fast as the other cases in 4000 yr. The mere fact that we do not observe pulsations is somewhat of concern but not completely unusual. To date, no pulsations have been found in the SGXB 4U1700-37 (Seifina et al. 2016) and in a few BeXBs (Reig 2011). New model calculations also show that at a moderate magnetic field strength of the order of 10^{11} G and a high inclination of the system (Brandt & Podsiadlowski 1995), pulsations are quite impossible to detect if the angle between the neutron star rotation and magnetic field axis is small (Falkner et al. 2019). We should also mention that Cumming (2008) proposed for the case of HETEJ 1900.1-2455 and possibly other accreting millisecond pulsars that B-fields can be partially buried, suppressing the observation of pulsations.

The fact that we know that the neutron star in Cir X-1 is very young combined with an identification of the companion as a B5Ia supergiant also can put some constraints on the evolutionary state of the entire binary. A formation scenario involving an AIC (Bhattacharya & van den Heuvel 1991) now seems highly unlikely. It also rules out that the progenitor star was a massive O-star as these only live less than 20 Myr, whereas B3 stars and later live more than 30 Myr (Behrend & Maeder 2001). Since the companion in Cir X-1 is in its supergiant phase, which the star is in during its very late main-sequence state, it must be much older than 20 Myr. More plausible is that the progenitor was quite similar to the companion, maybe one or two types earlier. This would put the progenitor into likely the lowest mass range (8–10 $M_{\odot}$) that can produce a neutron star. Today we know little about neutron star progenitor masses, and if this conclusion is true, it is quite extraordinary.

Last but not least, the classification of Cir X-1 as a BeXB might have the potential to at least partially explain the ∼30 yr transient flux behavior shown by Parkinson et al. (2003) by invoking a precession period for the Be-star–disk system. Such precession scenarios have already been suggested by Brandt & Podsiadlowski (1995) in terms of accretion disk precession and by Heinz et al. (2013) in terms of spin–orbit coupling effects between the neutron star spin and the binary orbit. Here we suggest a precession of a companion star disk. Superorbital periods in accretion disks are not unusual in X-ray binaries, as the examples of Her X-1, LMC X-4, and SMC X-1 show. Precessing Be-star disks are much more rare but not unheard of. Lau et al. (2016) recently reported on an apparent precessing helical outflow from the massive star WR102c. The interpretation is that the precessing outflow emerged from a previous evolutionary, rapidly rotating phase of the star and attributed the precession to an unseen compact companion. In a sense, this situation is not unsimilar to what we envision here. In the WR102c system, the period of the unseen companion was constrained to between 800 and 1400 days, which is much larger than the period in Cir X-1, but the precession period of 1.4×10^4 yr is very close to the long-term variation cycle in Cir X-1. This sets a precedent, and it is no longer a question whether it can happen, but it calls for details of how it happens.

We thank all members of the *Chandra X-Ray Center*, especially D. P. Huenemoerder and M. N. Nowak for their assistance with the HETG data processing and implementation of fitting procedures. Support for this project was provided by NASA through the Chandra Award GO7-18035X to MIT (N.S.S.), issued by the *Chandra X-Ray Observatory Center*, which is operated by the Smithonian Astrophysical Observatory for and on behalf of NASA under contract NAS8-03060.

ORCID iDs

T. E. Kallman https://orcid.org/0000-0002-5779-6906
S. Heinz https://orcid.org/0000-0002-8433-8652
P. Jonker https://orcid.org/0000-0001-5679-0695

References

Bautista, M. A., & Kallman, T. R. 2000, ApJ, 544, 581
Becker, P. A., & Wolff, M. T. 2007, ApJ, 654, 435
Behrend, R., & Maeder, A. 2001, A&A, 373, 190
Bhattacharya, D., & van den Heuvel, E. P. J. 1991, PhR, 203, 1
Bildsten, L. 1995, ApJ, 438, 852
Bildsten, L. 1998, ASIC, 515, 419
Brandt, N., & Podsiadlowski, P. 1995, MNRAS, 274, 461
Brandt, W. N., Fabian, A. C., Dotani, T., et al. 1996, MNRAS, 283, 1071
Brandt, W. N., & Schulz, N. S. 2000, ApJL, 544, L123
Caballero, I., & Wilms, J. 2012, MmSAI, 83, 230
Canizares, C. R., Davis, J. E., Dewey, D., et al. 2005, PASP, 117, 1144
Cash, W. 1979, ApJ, 228, 939
Clarkson, W. I., Charles, P. A., & Onyett, N. 2004, MNRAS, 348, 458
Coburn, W., Kretschmar, P., Kreykenbohm, I., et al. 2006, AdSpR, 38, 2747
Cumming, A. 2008, in AIP Conf. Ser. 1068, A Decade of Accreting Millisecond X-Ray Pulsars, ed. R. Wijnands (Melville, NY: AIP), 152
D'Aì, A., Bozzo, E., Papitto, A., et al. 2012, A&A, 543, A20
DeCesar, M. E., Boyd, P. T., Markwardt, C. B., et al. 2009, AAS Meeting Abstracts, 41, 299
Degenaar, N., Wijnands, R., Brown, E. F., et al. 2013, ApJ, 775, 48
Falkner, S. 2019, PhD Thesis, Friedrich-Alexander-Universität Erlangen-Nürnberg
Fender, R., Spencer, R., Tzioumis, T., et al. 1998, ApJL, 506, L121
Fujimoto, M. Y., Hanawa, T., & Miyaji, S. 1981, ApJ, 247, 267
Fürst, F., Suchy, S., Kreykenbohm, I., et al. 2011, A&A, 535, A9

Gagné, M., Oksala, M. E., Cohen, D. H., et al. 2005, ApJ, 628, 986
Glass, I. S. 1994, MNRAS, 268, 742
Gotthelf, E. V., & Halpern, J. P. 2007, ApJL, 664, L35
Gotthelf, E. V., & Halpern, J. P. 2009, ApJL, 695, L35
Gough, D. O., & Tayler, R. J. 1966, MNRAS, 133, 85
Halpern, J. P., & Gotthelf, E. V. 2010, ApJ, 709, 436
Halpern, J. P., Gotthelf, E. V., Camilo, F., & Seward, F. D. 2007, ApJ, 665, 1304
Heinz, S., Schulz, N. S., Brandt, W. N., & Galloway, D. K. 2007, ApJL, 663, L93
Heinz, S., Sell, P., Fender, R. P., et al. 2013, ApJ, 779, 171
Heinz, S., Burton, M., Braiding, C., et al. 2015, ApJ, 806, 265
Homan, J., van der Klis, M., Fridriksson, J. K., et al. 2010, ApJ, 719, 201
Iaria, R., D'Aí, A., Lavagetto, G., et al. 2008, ApJ, 673, 1033
Ji, L., Schulz, N., Nowak, M., Marshall, H. L., & Kallman, T. 2009, ApJ, 700, 977
Ji, L., Schulz, N. S., Nowak, M. A., & Canizares, C. R. 2011, ApJ, 729, 102
Jimenez-Garate, M. A., Raymond, J. C., & Liedahl, D. A. 2002, ApJ, 581, 1297
Jonker, P. G., & Nelemans, G. 2004, MNRAS, 354, 355
Jonker, P. G., Nelemans, G., & Bassa, C. G. 2007, MNRAS, 374, 999
Kallman, T. R., Palmeri, P., Bautista, M. A., Mendoza, C., & Krolik, J. H. 2004, ApJS, 155, 675
Kaluzienski, L. J., Holt, S. S., Boldt, E. A., & Serlemitsos, P. J. 1976, ApJL, 208, L71
Kaper, L., van der Meer, A., & Najarro, F. 2006, A&A, 457, 595
Kaspi, V. M. 2010, PNAS, 107, 7147
Koh, D. T., Bildsten, L., Chakrabarty, D., et al. 1997, ApJ, 479, 933
Lamb, F. K., Pethick, C. J., & Pines, D. 1973, ApJ, 184, 271
Lamers, H. J. G. L. M., Snow, T. P., & Lindholm, D. M. 1995, ApJ, 455, 269
Langer, N., Heger, A., & Fliegner, J. 1997, in IAU Symp. 189, ed. T. R. Bedding, A. J. Booth, & J. Davis, 343
Lau, R. M., Hankins, M. J., Herter, T. L., et al. 2016, ApJ, 818, 117
Linares, M., Watts, A., Altamirano, D., et al. 2010, ApJL, 719, L84
Margon, B., Lampton, M., Bowyer, S., & Cruddace, R. 1971, ApJL, 169, L23
Mirabel, I. F. 2001, ApSSS, 276, 319
Orlandini, M., Dal Fiume, D., Frontera, F., et al. 1998, ApJL, 500, L163
Özel, F., & Freire, P. 2016, ARA&A, 54, 401
Papitto, A., Riggio, A., di Salvo, T., et al. 2010, MNRAS, 407, 2575
Parkinson, P. M. S., Tournear, D. M., Bloom, E. D., et al. 2003, ApJ, 595, 333
Porquet, D., & Dubau, J. 2000, A&AS, 143, 495
Prinja, R. K., & Massa, D. L. 1998, in ASP Conf. Ser. 131, Properties of Hot Luminous Stars, ed. I. Howarth (San Francisco, CA: ASP), 218
Puls, J., Vink, J. S., & Najarro, F. 2008, A&ARv, 16, 209
Reig, P. 2011, Ap&SS, 332, 1
Rivinius, T., Carciofi, A. C., & Martayan, C. 2013, A&ARv, 21, 69
Sakurai, S., Torii, S., Noda, H., et al. 2014, PASJ, 66, 10
Sato, N., Nagase, F., Kawai, N., et al. 1986, ApJ, 304, 241
Schulz, N. S., & Brandt, W. N. 2002, ApJ, 572, 971
Schulz, N. S., Chakrabarty, D., Marshall, H. L., et al. 2001, ApJ, 563, 941
Schulz, N. S., Kallman, T. E., Galloway, D. K., & Brandt, W. N. 2008, ApJ, 672, 1091
Seifina, E., Titarchuk, L., & Shaposhnikov, N. 2016, ApJ, 821, 23
Sell, P. H., Heinz, S., Calvelo, D. E., et al. 2010, ApJL, 719, L194
Shabaltas, N., & Lai, D. 2012, ApJ, 748, 148
Shirey, R. E., Bradt, H. V., & Levine, A. M. 1999, ApJ, 517, 472
Shirey, R. E., Bradt, H. V., Levine, A. M., & Morgan, E. H. 1998, ApJ, 506, 374
Stewart, R. T., Caswell, J. L., Haynes, R. F., & Nelson, G. J. 1993, MNRAS, 261, 593
Stewart, R. T., Nelson, G. J., Penninx, W., et al. 1991, MNRAS, 253, 212
Tauris, T. M., Fender, R. P., van den Heuvel, E. P. J., Johnston, H. M., & Wu, K. 1999, MNRAS, 310, 1165
Tauris, T. M., Sanyal, D., Yoon, S.-C., & Langer, N. 2013, A&A, 558, A39
Tennant, A. F. 1987, MNRAS, 226, 971
Tennant, A. F., Fabian, A. C., & Shafer, R. A. 1986, MNRAS, 221, 27P
Watanabe, S., Sako, M., Ishida, M., et al. 2003, ApJL, 597, L37
Whelan, J. A. J., Mayo, S. K., Wickramasinghe, D. T., et al. 1977, MNRAS, 181, 259